Remote Sensing of Environment 114 (2010) 1777–1790

Contents lists available at ScienceDirect

Remote Sensing of Environment

journal homepage: www.elsevier.com/locate/rse

Retrieval of subpixel *Tamarix* canopy cover from Landsat data along the Forgotten River using linear and nonlinear spectral mixture models

J.L. Silván-Cárdenas *, L. Wang

Department of Geography, University at Buffalo, The State University of New York, 105 Wilkeson Quad., Buffalo, NY 14261, USA

ARTICLE INFO

Article history:
Received 1 October 2008
Received in revised form 30 March 2010
Accepted 3 April 2010

Keywords:
Tamarix
Spectral unmixing
Multiple scattering
Subpixel confusion

ABSTRACT

Repeatable approaches for mapping saltcedar (*Tamarix* spp.) at regional scales, with the ability to detect low density stands, is crucial for the species' effective control and management, as well as for an improved understanding of its current and potential future dynamics. This study had the objective of testing subpixel classification techniques based on linear and nonlinear spectral mixture models in order to identify the best possible classification technique for repeatable mapping of saltcedar canopy cover along the Forgotten River reach of the Rio Grande. The suite of methods tested were meant to represent various levels of constraints imposed in the solution as well as varying levels of classification details (species level and landscape level), sources for endmembers (space-borne multispectral image, airborne hyperspectral image and *in situ* spectra measurements) and mixture modes (linear and nonlinear). A multiple scattering approximation (MSA) model was proposed as a means to represent canopy (image) reflectance spectra as a nonlinear combination of subcanopy (field) reflectance spectra. The accuracy of subpixel canopy cover was assessed through a 1-m spatial-resolution hyperspectral image and field measurements. Results indicated that: 1) When saltcedar was represented by one single image spectrum (endmember), the unconstrained linear spectral unmixing with post-classification normalization produced comparable accuracy (OA = 72%) to those delivered by partially and fully constrained linear spectral unmixing (63–72%) and even by nonlinear spectral unmixing (73%). 2) The accuracy of the fully constrained linear spectral unmixing method increased (from 67% to 77%) when the classes were represented with several image spectra. 3) Saltcedar canopy reflectance showed the strongest nonlinear relationship with respect to subcanopy reflectance, as indicated through a range of estimated canopy recollision probabilities. 4) Despite the considerations of these effects on canopy reflectance, the inversion of the nonlinear spectral mixing model with subcanopy reflectance (field) measurements yielded slightly lower accuracy (73%) than the linear counterpart (77%). Implications of these results for region-wide monitoring of saltcedar invasion are also discussed.

1. Introduction

Invasive species threats, which have been recognized as an important component of global environmental change (Drake et al., 1989; Vitousek et al., 1996), demand effective analysis with regional-scale remote sensing measurements. The invasion of saltcedar (*Tamarix* spp.) in the southwestern United States and northern Mexico represents a high priority case, in which remote sensing data plays a crucial role in both management operations and understanding the invasion process (Hunt et al., 2003; Lass et al., 2005). However, the analysis of moderate spatial resolution imagery (10–100 m) that is required for addressing the invasion problem still encounters a number of challenges. For example, recent studies of spectral invariants in canopy radiative transfer functions proposed a simple parameterization of the light–canopy interaction that would allow more accurate estimations of the canopy cover (Huang et al., 2007; Lewis & Disney, 2007; Smolander & Stenberg, 2005). These nonlinear mixture models are, however, difficult to invert, and their application with moderate-resolution imagery is still to be assessed. These issues motivated the present study.

Previous studies have shown that saltcedar habitats can be mapped using remotely sensed data and techniques (1996; Carruthers et al., 2006; Everitt & DeLoach, 1990, Everitt et al., 1992; Hamada et al., 2007). Approaches coupling high spatial resolution and hyperspectral images with conventional pixel-level classifications can achieve high accuracies (Carruthers et al., 2006; Hamada et al., 2007). Such images, however, tend to cover only small areas on the ground and are expensive to acquire, thus limiting their utility for macro-scale monitoring. The application of moderate resolution satellite images, which cover larger areas on the ground, are advantageous in this respect. In recent studies, NASA's Moderate Resolution Imaging Spectroradiometer (MODIS) was successfully used for mapping

* Corresponding author.
E-mail addresses: jlsilvan@buffalo.edu (J.L. Silván-Cárdenas), lewang@buffalo.edu (L. Wang).

0034-4257/$ – see front matter © 2010 Elsevier Inc. All rights reserved.
doi:10.1016/j.rse.2010.04.003

saltcedar habitat suitability at the regional scale (Morisette et al., 2006). The relatively low spatial resolution of MODIS data, however, makes it impossible to detect accurately low-density saltcedar stands (e.g., early invasion stage). In another study along the Arkansas River in Colorado, the near-infrared bands of Landsat TM data have been found effective for discriminating large patches of saltcedar during the leaf-off season (Groeneveld & Watson, 2008). One obvious limitation for moderate-resolution sensors, however, is the difficulty in accurately detecting small extents of saltcedar invasion, which is crucial for effective management (Shafroth et al., 2005). Yet, because the width of saltcedar bands along the river typically varies from a few meters to hundreds of meters, Landsat measurements represent a good compromise between spatial resolution and spatial extent for mapping the distribution of saltcedar. This study hypothesized that the use of subpixel classification methods would further enhance the utility of Landsat data for tackling the saltcedar invasion problem.

Subpixel classification techniques are superior to traditional pixel-level classifications techniques because they allow for the quantification of subpixel species coverage. Three major approaches for subpixel classification have been identified (Eastman & Laney, 2002): 1) spectral mixture analysis (SMA), 2) regressive approaches, such as neural networks, and 3) soft classification methods based on fuzzy sets and probability theories. This study focused on the first approach. The rationale of SMA is that mixed pixels result from a systematic combination of component spectra (endmembers) present in the sensor's instantaneous field of view (IFOV) (Adams et al., 1993; Gillespie, 1992; Milton, 1999. The relative contribution of component spectra is then determined by the inversion of mixture models (Chang & Heinz, 2000; Heinz & Chang, 2001; Hu et al., 1999; Keshava & Mustard, 2002).

The mathematical form of the mixture model is strongly influenced by the definition of the endmembers. While the horizontal mixing of vegetation types across the landscape due to an increase in the IFOV with respect to plant canopy is primarily a linear process (Adams et al., 1995; Roberts et al., 1993), the interaction of light with vegetation components (i.e., leaves, stems, etc.) in the three-dimensional space is highly nonlinear (Borel & Gerstl, 1994; Ray & Murray, 1996; Smolander & Stenberg, 2005). The assumption of a linear mixture process is convenient because the endmembers are, by definition, confined to the extremes of the mixing space (Boardman et al., 1993; Small, 2004). For vegetation mapping, however, the endmembers thus defined may be meaningless or hard to match with ground measurements due to nonlinear mixing processes. Recent studies on canopy radiative transfer functions have led to the development of the canopy spectral invariant theory (Huang et al., 2007; Knyazikhin et al., 1998; Lewis & Disney, 2007), according to which variations of canopy scattering (reflectance plus transmittance) and absorptance are mainly influenced by optical properties (spectral leaf transmittance and reflectance) of individual leaves and two wavelength independent canopy structural variables: the canopy interceptance and the recollision probability. Based on this theory, explicit mathematical relationships of the light–canopy interaction have been developed for single homogeneous canopies with non-reflective background (Smolander & Stenberg, 2005). Interestingly, the algebraic structure of these models holds across multiple mixing scales, from needle/leaf to shoot/branch and from shoot/branch to canopy (2005; Lewis & Disney, 2007, Smolander & Stenberg, 2003). This study hypothesized that proper inversion of this kind of model should lead to improved estimations of subpixel canopy cover of saltcedar.

The general objective of this study was to test linear and nonlinear spectral mixture models in order to identify the best possible classification strategy for repeatable mapping of saltcedar on a regional setting. The specific objectives were:

(1) Assess the role of multiple scattering on canopy reflectance using a modeling approach,
(2) Test whether the level of constraint imposed in the least square inversion of the linear mixture model plays a major role in the accuracy of estimated subpixel canopy coverage,
(3) Determine whether the thematic level at which endmembers are defined has a significant impact on subpixel canopy cover estimations,
(4) Test whether the consideration of the multiple scattering phenomena can lead to increased accuracy in estimating subpixel saltcedar canopy coverage from Landsat data.

In order to attain the above objectives, seven subpixel classification methods were tested. Five of these methods were based on the linear mixture model with varying levels of constraint (unconstrained, sum-constrained, nonnegativity-constrained, fully constrained, and tessellated linear spectral unmixing, Section 3.1). The other two methods were based on a nonlinear mixture model (the fully constrained and the tessellated multiple scattering approximation spectral unmixing methods, Section 3.2). The suite of methods tested involved three spectral libraries that represented three levels of detail: level 1 of a classification system (L1ETM, Section 3.1.2), level 2 with canopy measurements (L2AISA, Section 3.1.2), and level 2 with subcanopy measurements (L2SYNTH, Section 3.2.4).

2. Data used

The study incorporated three data sources for derivation of reference fractions and endmember reflectance spectra (Fig. 1): 1) a Landsat ETM+ image (Section 2.2), 2) an airborne hyperspectral image (Section 2.2), and 3) *in situ* measurements (Section 2.3). The rest of this section provides details on the processing and role of these data sets.

2.1. Study site

A study site was selected on the Forgotten River reach of the Rio Grande River near the town of Candelaria, Texas (Fig. 2). At this site, the riverbanks have been taken over by saltcedar, and the native cottonwood (*Populus* spp) that once dominated the area is completely absent (Everitt, 1998). The vegetation on both banks of the river is composed mostly of saltcedar (*Tamarix chinensis* L.) with some mixes of willow (*Salix* spp). The spatial distribution of saltcedar along the river is variable, due in part to differences in the local hydrologic system. As one moves into the uplands, honey mesquite (*Prosopis* spp) stands are found, although they are generally mixed with other weeds and saltcedar. A giant saltcedar species (*Tamarix aphylla* L. Karst or Athel tamarisk) is also found in the study site, although in very sparse occurrences along the uplands.

2.2. Image acquisition and processing

The Airborne Imaging Spectroradiometer for Applications (AISA) sensor system (Spectral Imaging LTD) was flown over the study site on 21 December 2005. The acquisition time coincided with the time window when saltcedar's foliage turns a yellow-orange to orange-brown color before leaf drop and thus can be more easily discriminated from native mesquite and willow species (Everitt & DeLoach, 1990). The AISA imagery acquired had 61 bands in the spectral range 400–1000 nm with an average full width at half maximum (FWHM) of 9.5 nm and spatial resolution of 1 m. The AISA digital numbers represented reflectance values (times a multiplier) that had been corrected from geometric and radiometric distortions. Five image strips of 10-km length and 1-km swath were used to create a mosaic image, from which a subset of 2.3-km by 10-km was extracted.

The AISA image showed a strong absorption feature around 934 nm (water vapor absorption) and a weaker absorption feature

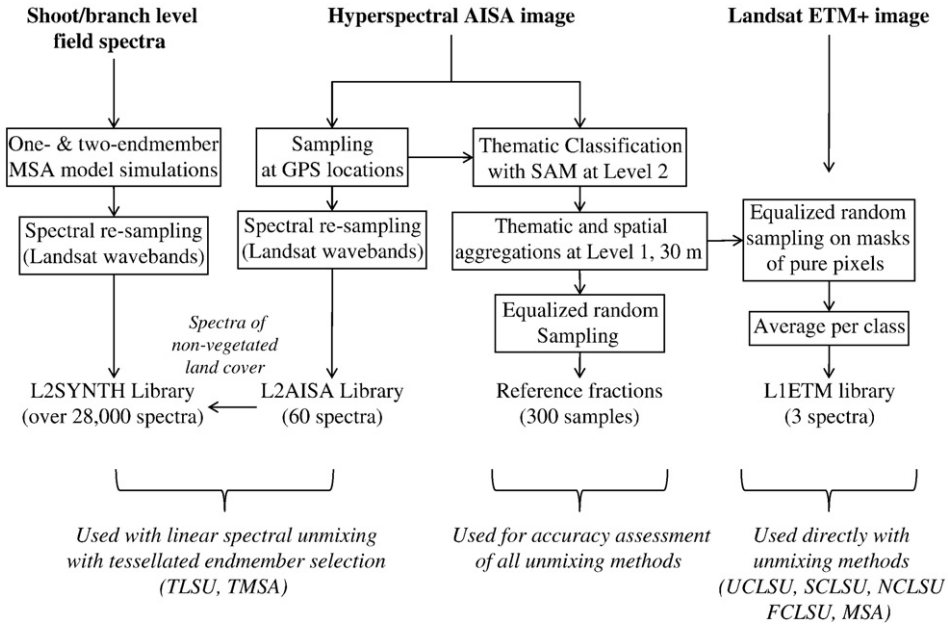

Fig. 1. Major processing steps for generating the ground-truth fractional cover at 30-m spatial resolution and canopy reflectance spectra at the Landsat spectral resolution.

around 750 nm (ozone absorption). These absorption features were eliminated by matching the reflectance spectra of a patch of dry grass measured in the field with its corresponding reflectance from the image. Since the scatterplot between the two spectra, for wavelengths lower than 732 nm, formed a nearly perfect straight line ($R^2 = 0.998$), it was assumed that the recalibration would not affect our analysis on multiple scattering.

A Landsat 7 ETM+ image (path 31, row 39) acquired in the Scan Line Corrector (SLC)-off mode on 19 December 2005 was used in this study. The SLC is an electromechanical device that compensates for the forward motion of the satellite, but since it was turned off due to a failure in May 2003, the ETM+ line of sight now traces a zigzag pattern along the satellite ground track. The image was ordered with a gap-fill processing, according to which missing pixels are populated with histogram-matched data from one or more images acquired at anniversary dates (see http://eros.usgs.gov/products/satellite/landsat7.php for further details). Despite the data gaps, no striping was apparent in the subset of the study site. However, an atmospheric correction processing was necessary in order to reduce the effects of thin cirrus clouds present on the central part of the subset. For this purpose, the Fast Line-of-sight Atmospheric Analysis of Spectral Hypercubes (FLAASH) algorithm built into the ENVI system (ITT Visual Information Solutions) was used. The FLAASH program produced at-surface reflectance through the definition of built-in atmospheric (U.S. standard) and aerosol (Rural) models with default settings.

In order to ensure a consistent radiometric scale between the Landsat and the AISA images, the Landsat image was registered and

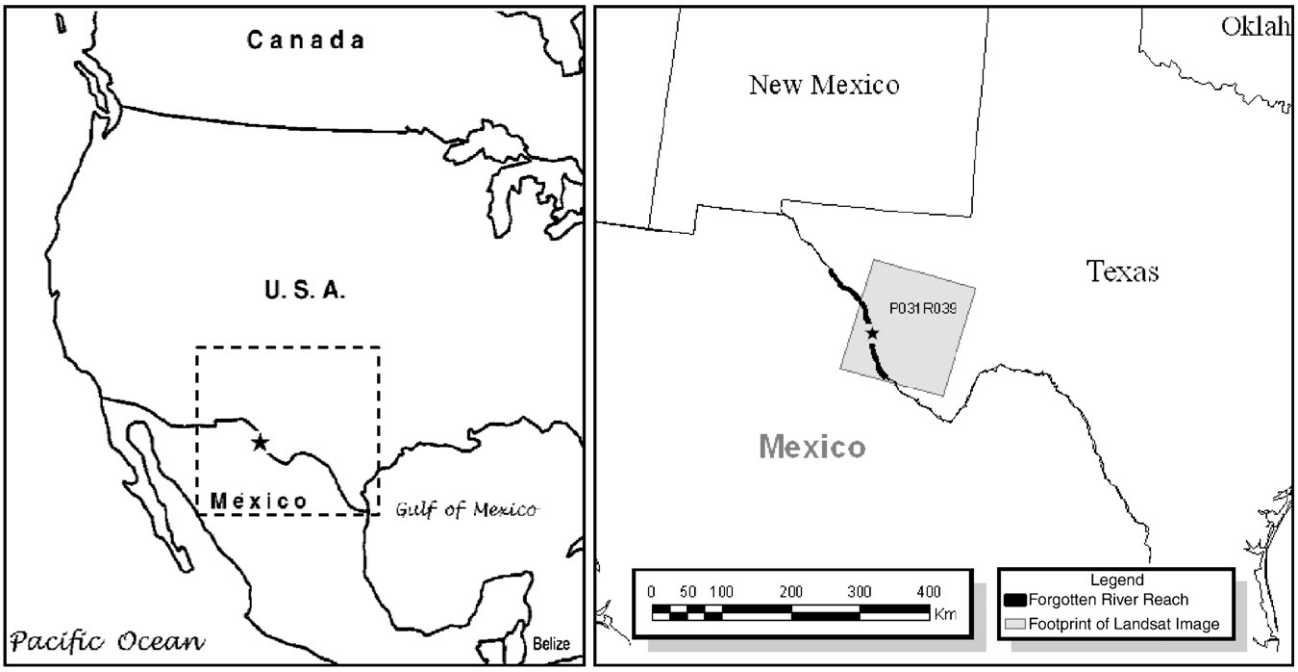

Fig. 2. Geographic location of the study site.

recalibrated using a synthetic image derived from the AISA image. The synthetic Landsat image was produced by applying spectral and spatial resampling tools to the AISA imagery. The spectral resampling used ENVI's built-in filter functions for Landsat ETM+ bands, whereas the spatial resampling used an average filter function. Since the spectral range covered by AISA (and also by the field spectra) overlapped with Landsat bands 1 through 4 (i.e., blue, green, red, and NIR spectral bands), only bands 1–4 of the Landsat image were used. These wavebands have been shown effective for saltcedar discrimination considering the acquisition date (Everitt & DeLoach, 1990). The four Landsat bands were co-registered to the synthetic image through pairing of on-screen collected ground control points ($n = 14$, $RMSE = 0.38$). After the co-registration, a radiometric recalibration was carried out using the synthetic Landsat image as reference. The recalibration of the reflectance values further reduced the atmospheric effects on shorter wavelength bands. Specifically, the slope of the linear transformation ranged from 0.74 for band 1 (blue band) to 1.0 for band 4 (NIR band).

2.3. Canopy and subcanopy reflectance measurements

Canopy and subcanopy reflectance measurements were acquired through field sampling and from the AISA imagery (Fig. 3). In order to link field observations to image observations, a two-level classification system was defined. Table 1 summarizes the two-level classification system used in this study.

Two field trips (Nov. 17–19, 2004, Dec. 17–19, 2005) were arranged to collect sufficient ground truthing data in the study site. Locations of target species and non-vegetated features were measured with a hand-held global positioning system (GPS Trimble GeoXM). The unit is accurate to 1–3 m. Both points and polygon features were recorded for each target species (46 points and 31 polygons in total). Point features were acquired near the main trunk of trees using an extendable pole that lifted the GPS antenna up to 4 m above the ground. Polygons and points acquired in the field were overlaid on true color and color-infrared composites of the AISA image, and a manual selection of smaller polygons was performed in order to correct for any spatial misalignment. Additional polygons were also added for non-vegetated land cover classes based on on-screen identification. Canopy reflectance measurements were then produced by averaging the AISA reflectance values within selected polygons and classified at level 2 of the classification system (Table 1).

Table 1
Two-level classification system used in the study.

Class level 1	Class level 2	Description
1. Invasive (*Tamarix*)	1. Green saltcedar	*Tamarix* dominated by green and brown foliage
	2. Senescent saltcedar	*Tamarix* dominated by orange foliage
	3. Dry saltcedar	*Tamarix* dominated by pale frosted leaves
2. Native (woody riparian species)	4. Leaf on willow	*Salix* spp. with leaves on
	5. Leaf-off willow	*Salix* spp. with few leaves on
	6. Leaf on mesquite	*Prosopis* spp. with leaves on
	7. Leaf-off mesquite	*Prosopis* spp. with few leaves on
	8. Poverty weed	*Iva* spp. with greenish leaves
3. Other (non-woody vegetation and other land-cover types)	9. Creosote bush[a]	Short bush, sparsely distributed along hillside
	10. Herbaceous-dry	Primarily dormant grasses, but includes herbaceous weedy plants
	11. Herbaceous-green	Green herbaceous plants
	12. Wetland	Emergent herbaceous wetlands
	13. Water	River, pond or lake water
	14. Soil	Sandy bare ground
	15. Gravel	Barren gravel and gravel road
	16. Road	Asphalt paved road
	17. Roof	Any kind of house roof

[a] Creosote bush was not included in the class Native as it occurs in the hilly region, i.e., it is non-riparian.

The second field campaign was concurrent with the AISA image acquisition and hence was more appropriate for spectral reflectance measurements. Reflectance measurements were taken using a hand-held spectroradiometer (Analytical Spectral Device UV/VNIR). The device had fiber optic cable input 1.2 m in length with 25° full angle cone of acceptance field-of-view. This instrument provides reflectance spectra at the spectral resolution of 1 nm in the UV/VNIR range (350–1050 nm). Subcanopy reflectance measurements were made by pointing the fiber optic cable input vertically towards sun-illuminated branches at breast height. Each target was measured ten times, and

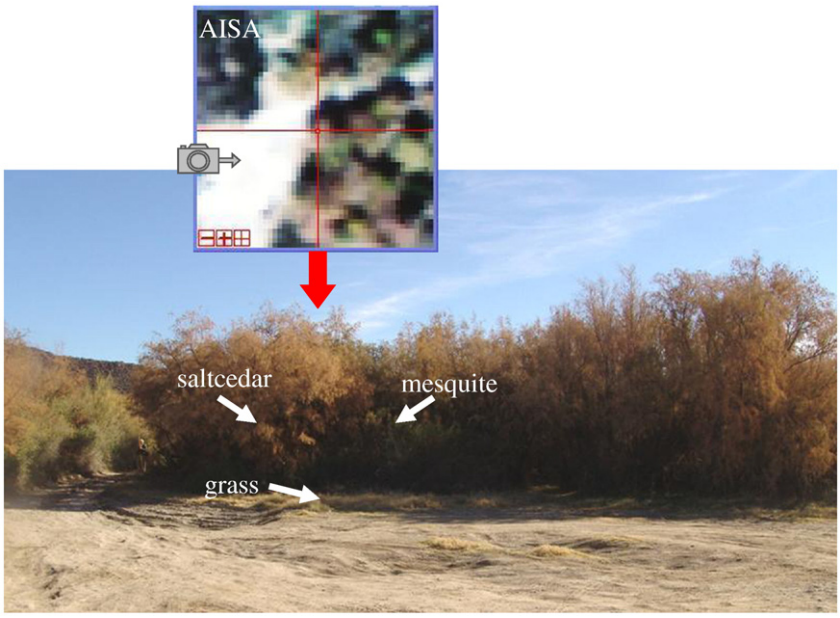

Fig. 3. This figure shows the approximate locations of some canopy (red arrow) and subcanopy (white arrows) reflectance spectra measurements used in the study.

measurements were averaged to reduce effects from variations in illumination, movement of branches by wind and/or intrinsic noise from equipment. The sky was nearly cloud-free at the time of data acquisition, which occurred from 11 a.m. to 2 p.m. (local time).

Sample sizes from both image and field measurements are provided in Table 2. The AISA image-based reflectance spectra are hereafter referred to as canopy spectra, whereas the spectroradiometer reflectance measurements are referred to as subcanopy spectra. For the purpose of analysis, subcanopy spectra were resampled to match the spectral resolution of canopy spectra (from 1 nm to around 10 nm). Fig. 4 provides example plots for subcanopy and canopy reflectance spectra for various classes.

2.4. Reference fractions

Due to the intrinsic difficulties of collecting ground-truth fractional coverage in the field, reference fractions were derived from the AISA image (Fig. 1). The AISA image was classified at classification level 2 using the spectral angle mapper (SAM) classification method (Kruse et al., 1993). This classification method requires a spectral library of classified spectra, each of which is compared with the image spectra via the spectral angle, i.e. the angle formed between two spectra of n bands when considered as vectors of n dimensions. SAM assigns the class with the smallest angle to the image spectra. The canopy spectra acquired with the aid of GPS points (Table 2) were used for this purpose. The SAM classification result was then aggregated to the classification level 1 and class masks extracted. The reference fractions were produced by aggregating the class masks at 30-m resolution (Fig. 5). The accuracy of the reference fraction layer could not be quantified but was assumed high (say above 90%) given the spectral and spatial resolution of the AISA image, the relatively large number of training spectra (60), and because the dominant class (on 31 polygons) matched perfectly the primary land cover recorded in the field.

A sample set of 300 points was randomly drawn for accuracy assessment. At each sampled site, four reflectance values from Landsat bands and associated subpixel fractions for Invasive, Native, and Other categories were recorded. 100 samples were drawn for each land cover class where that particular class was dominant, i.e. had the largest land cover fraction. This equalized sampling scheme was used in order to ensure that no class contributed more than the others to the accuracy or error measures.

Table 2
Number of spectral reflectance samples available for each class.

Target name	Field spectra	Image spectra
Green saltcedar	5	4
Senescent saltcedar	5	4
Dry saltcedar	4	3
Invasive total	14	11
Leaf on willow	2	4
Leaf-off willow	2	1
Leaf on mesquite	6	2
Leaf-off mesquite	4	3
Poverty weed	4	2
Native total	18	12
Creosote bush	8	1
Herbaceous-dry	5	6
Herbaceous-green	0	2
Wetland	0	5
Water	0	11
Soil	0	1
Gravel	0	5
Road	0	2
Roof	0	4
Other total	13	37
Overall total	45	60

3. Subpixel classification methods

This section summarizes the methods tested in the study. The two nonlinear spectral unmixing methods described in Section 3.2 and the tessellated linear spectral unmixing presented in Section 3.1.3 represent methodological contributions from this study. In all the cases, the purpose was to derive subpixel classifications at level 1 of the classification system in Table 1.

3.1. Linear spectral unmixing

For an image with n bands and m different cover types, the linear mixture model is expressed in matrix form as:

$$\mathbf{y} = \mathbf{X}\alpha + \varepsilon \tag{1}$$

where $\mathbf{y}=[y_1 \cdots y_n]^T$ is the mixed pixel, $\alpha=[\alpha_1 \cdots \alpha_m]^T$ is the subpixel fractional cover, $\mathbf{X}$ is an $n \times m$ matrix containing m endmember spectra as column vectors, and ε is the residual not explained by the linear model.

If $\mathbf{y}$ and $\mathbf{X}$ are known, α is usually estimated through an ordinary least square (OLS) optimization procedure. The OLS optimization estimates α by minimizing the magnitude of the residual between the observed mixed pixel and the corresponding model mixed pixels for a given set of endmembers. Otherwise stated:

$$\min_{\alpha} \|\mathbf{y}-\mathbf{X}\alpha\|^2 \tag{2}$$

subject to:

$$i)\ 1^T\alpha = 1$$
$$ii)\ \alpha \geq 0$$

where $\mathbf{1}$ and $\mathbf{0}$ are column vectors of m ones and m zeros, respectively.

Researchers have noted that the sum constraint (i) above is easy to implement, but the nonnegativity constraint (ii) is not (Chang & Heinz, 2000; Heinz & Chang, 2001; Hu et al., 1999). As a result, most studies only implement the sum constraint in the model and then apply the nonnegativity constraint to the results. This study sought to test unconstrained, partially constrained and fully constrained optimizations and assess the accuracy and relative efficiency of each method.

3.1.1. Constraint level

If the two constraints are ignored, the solution is given by Eq. (3) (Ravishanker & Dey, 2002):

$$\alpha_{UC} = \left(\mathbf{X}^T\mathbf{X}\right)^{-1}\mathbf{X}^T\mathbf{y} \tag{3}$$

This method is hereafter referred to as unconstrained least squares LSU or simply UCLSU. When the sum constraint is considered alone, the solution can be found through the Lagrange multiplier method (Heinz & Chang, 2001; JJ & Drake, 1993). This solution is provided in Eq. (4), where $\mathbf{G}=(\mathbf{X}^T\mathbf{X})^{-1}$ and α_{UC} is the solution to the unconstrained problem above (Eq. (3)):

$$\alpha_{SC} = \alpha_{UC} - \mathbf{G}1\left(1^T\mathbf{G}1\right)^{-1}\left(1^T\alpha_{UC}-1\right) \tag{4}$$

This method is hereafter referred to as sum-constrained LSU or SCLSU.

The other two formulations considered here, which fulfill the nonnegativity constraint, do not have exact mathematical solutions. If the nonnegativity constraint is considered alone, the solution is termed the nonnegativity-constrained LSU or NCLSU. In this case, an iterative procedure based on Lagrange multiplier optimization is

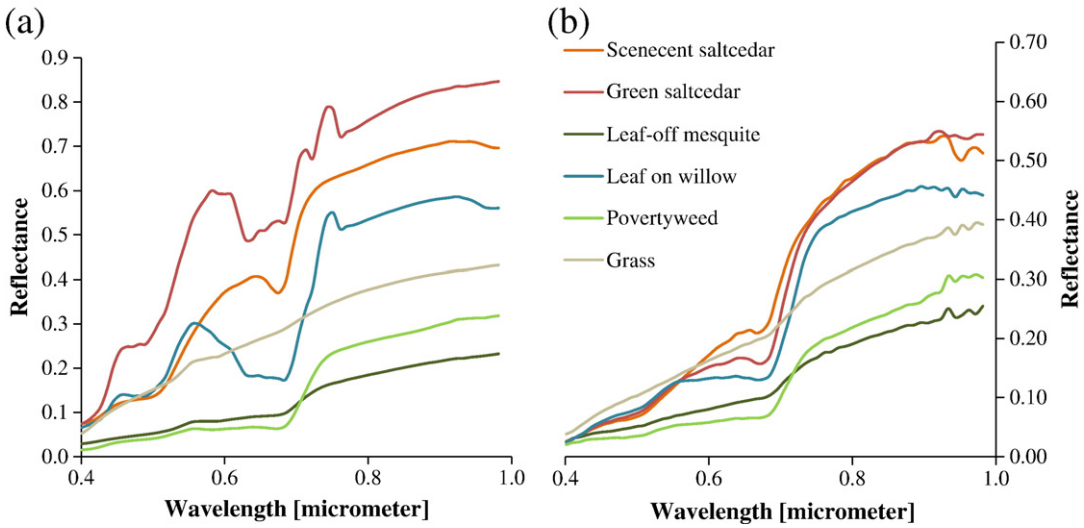

Fig. 4. Examples of subcanopy (a) and canopy (b) reflectance spectra of major vegetation species in the study site. Subcanopy spectra correspond to spectroradiometer measurements at branch level, whereas canopy spectra correspond to airborne hyperspectral (AISA) measurements.

necessary (Chang & Heinz, 2000). In this study, a LSQNONEG optimization routine available in the MATLAB optimization toolbox was used (The MathWorks, Inc., 2002). LSQNONEG required an initial solution, which was set to the unconstrained solution above (Eq. (3)). Details on the LSQNONEG optimization algorithm are provided in Lawson and Hanson (1974).

Likewise, the fourth formulation is here referred to as the fully constrained least squares LSU or simply FCLSU. The fully constrained problem can be alternatively expressed as a quadratic program (Heinz & Chang, 2001; Hu et al., 1999). A QUADPROG function in the optimization toolbox of the software package MATLAB was used with the unconstrained solution as the initial solution. The QUADPROG

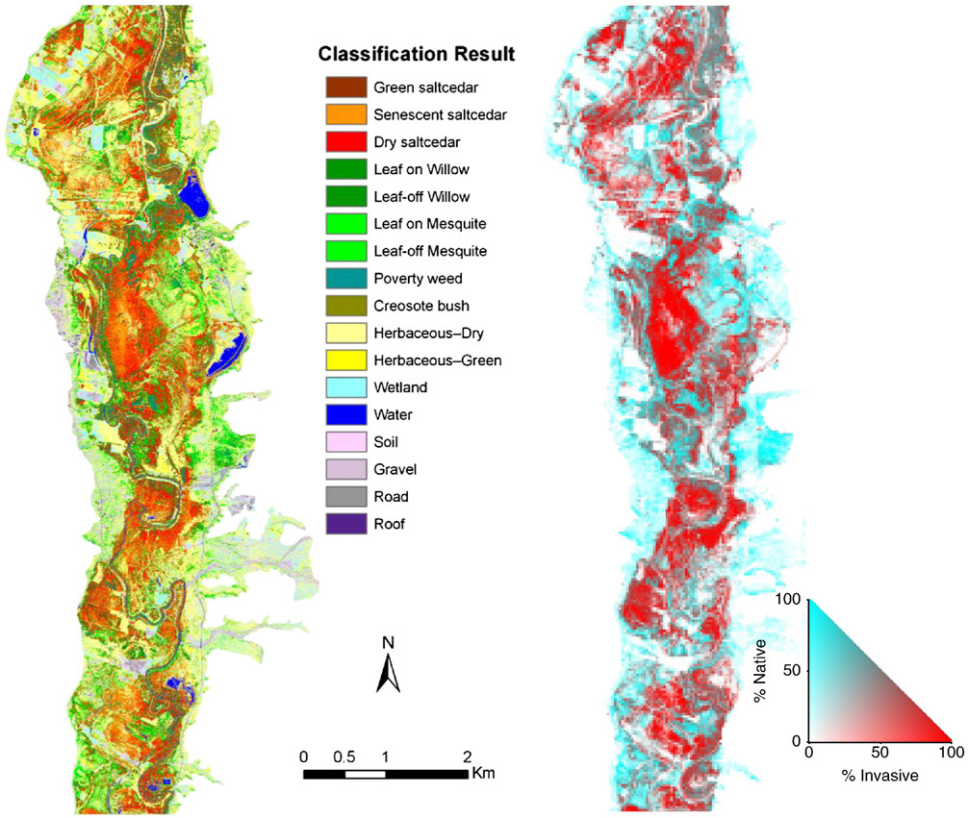

Fig. 5. Classification map obtained through spectral angle mapper (SAM) classification of AISA imagery at 1-m spatial resolution (left) and map of derived subpixel fractional coverage at 30-m spatial resolution (right). In the latter case, full subpixel coverage of class Invasive is shown in an intense red tone, full subpixel coverage of class Native is shown in an intense cyan tone, and full subpixel coverage of class Other is shown in white. Combinations of the three land cover classes yield intermediate tones. The large red patches are likely to correspond with established stands of saltcedar that have monopolized the space, whereas smaller patches (pink and dark cyan tones) should correspond with incipient saltcedar invasion or areas where saltcedar remains a sub-dominant species (Sher et al., 2002).

algorithm involves two phases. The first phase involves the calculation of a feasible point (if one exists). The second phase involves the generation of an iterative sequence of feasible points that converge to the solution. The reader is referred to (Gill et al., 1991) and to the software documentation for further details on this optimization algorithm.

3.1.2. Endmember definition for LSU

Two endmember definitions were tested with the linear mixture model. Both definitions were based on image data (image endmembers), as they are most likely linearly mixed. In the first strategy, endmembers were produced at level 1 by averaging Landsat spectra from pixels with land-cover fractions greater than 0.95 in the reference fractions (see Fig. 1). Since fractions were already aggregated at the thematic level 1, there were only three endmembers in this case: one for Native, one for Invasive and one for Other. The collection of these image spectra is hereafter referred to as L1ETM. This definition of endmembers contrasts the generic definition proposed for arid landscapes (Asner & Heidebrecht, 2002; Roberts et al., 1993), which considers photosynthetic vegetation (PV), non-photosynthetic vegetation (NPV) and bare soil as endmembers.

The generalization of endmembers above is convenient because the intrinsic dimension of the data limits the maximum number of endmembers that can be considered simultaneously for model inversion. Such generalization may, however, imply significant spectral variability within each class (intra-class variability) and neglect the spatial variability of endmembers. To circumvent these issues, several alternatives have been developed that involve various endmember selection strategies (Carpenter et al., 1999; Dennison & Roberts, 2003; Miao et al., 2006; Okin et al., 2001; Plaza et al., 2004; Roberts et al., 1992, 1998; Smith et al., 1994. Most of these techniques are computationally intensive and are more appropriate for hyperspectral data. The alternative adopted here combines a level 2 definition of endmembers with an automatic selection algorithm based on concepts of convex geometry (Boardman et al., 1993). The spectral library used in this case was derived from the AISA image, and thus is hereafter referred to as L2AISA. The L2AISA library consisted of the 60 spectra that were used for classifying the AISA image, but resampled at the spectral resolution of the Landsat image (see Fig. 1). The endmember selection strategy adopted was based on a tessellation, as described in the following subsection. Hence, the unmixing method is hereafter referred to as the tessellated linear spectral unmixing (TLSU).

3.1.3. Tessellated linear spectral unmixing (TLSU)

For the TLSU method, a Delaunay tessellation of the entire set of endmembers was built by considering each library spectrum as a point of the n-dimensional Euclidian space. Such a tessellation partitions the mixing space into polyhedra called simplices. A simplex is a generalization of the concept of triangle in two-dimensional space, or tetrahedron in three-dimensional space. The parts of a simplex are called vertices or 0-facets, edges or 1-facets, faces or 2-facets, cells or 3-facets or, in general, r-facet, for $r = 0, \ldots, n$.

If mixed pixels are also considered points of the n-dimensional space, and the Euclidian distance is the spectral proximity measure, then the vertices of the closest simplex to a point represent reasonably good candidates for endmembers of the mixed pixel represented by the point. Based on this spectral proximity criterion, we selected for each mixed pixel the $n+1$ vertices of the simplex enclosing the point (see Fig. 6 for a geometric interpretation). Consequently, the mixture fractions correspond to the barycentric coordinates of the point with respect to the selected simplex (Boardman et al., 1993). One exception occurs if the point falls outside the convex hull. In such cases, there is no simplex enclosing the pixel, and the most spectrally similar endmembers correspond to the vertices of the nearest facet of the convex hull. Instead of searching for such facets, it was found more convenient to consider the fully constrained least squares solution with endmembers that correspond to vertices of the convex hull. In this way, the optimization routine assigns nonzero fractions to the endmembers that form the nearest facet and zero fractions to all other endmembers.

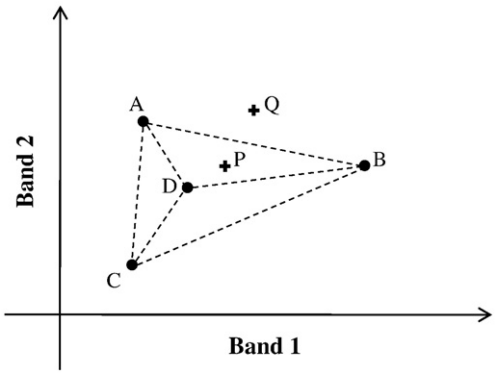

Fig. 6. Geometric interpretation of the tessellated linear spectral unmixing (TLSU) method for four endmembers with two bands. A, B, C and D represent endmembers, whereas P and Q represent mixed pixels. The discontinuous lines indicate the Delaunay tessellation defining the endmember selection criterion. Pixel P is unmixed using the vertices of the closest simplex (triangle ABD), whereas Q is unmixed using the vertices of the convex hull (triangle ABC). Although the endmember D is interior to the mixing space of endmembers A, B and C, it cannot be considered a combination of the latter (see, for example, Fig. 9 for the relative location of leaf-on willow, which can play the role of D, and green saltcedar, poverty weed and grass, which can play the roles of A, B and C, respectively, in the PC1–PC2 plane). This situation is likely to happen when using broadband spectra such as Landsat TM.

A TLSU function was written in MATLAB programming language. This function used available implementations of the Delaunay tessellation (DELAUNAYN) and the simplex search methods (TSEARCHN). These programs are based on the efficient QUICKHULL algorithm developed by Barber et al. (1996). The TLSU function takes advantage of the calculation of the barycentric coordinates by TSEARCH for interior pixels, while it uses the QUADPROG optimization routine for unmixing pixels that fall outside the convex hull. The TLSU function arranges the fractions in a sparse matrix (one column per mixed pixel and one row per endmember) and then multiplies it by an aggregation matrix (one column per endmember and one row per class) that is passed by the user. The aggregation matrix defines the membership relationship between endmembers and classes. In this way, TLSU delivered fractions at classification level 1 from endmembers defined at level 2. The result after aggregation is comparable to considering endmember bundles (Bateson et al., 2000).

3.2. Nonlinear spectral unmixing

A nonlinear spectral mixture model was developed to account for effects of the multiple scattering phenomena in canopy reflectance. The model development builds upon results from the spectral invariant theory, according to which leaf/shoot reflectance is related to canopy reflectance through photon recollision probability parameters (Huang et al., 2007; Lewis & Disney, 2007; Smolander & Stenberg, 2005). The description of the model is presented below followed by two spectral unmixing methods based on the model.

3.2.1. The multiple scattering approximation (MSA) model

Considering a homogeneous canopy composed of leaves only and bounded at the bottom by a black surface, the canopy scattering $y(\lambda)$ at wavelength λ is related to the leaf scattering $x(\lambda)$ through a nonlinear model of the form (Smolander & Stenberg, 2005):

$$y(\lambda) = \alpha \frac{(1-p)x(\lambda)}{1-px(\lambda)} \tag{5}$$

where α denotes the canopy interceptance, i.e., the portions of photons intercepted by the canopy, and p denotes the photon recollision probability, i.e., the mean probability that a photon scattered from a leaf in the canopy will interact with the canopy again. Consequently, $1-p$ is the photon escaping probability, and $1-\alpha$ is the portion of photons transmitted directly to the ground.

The photon–canopy interaction can be conceptualized as a closed system with a positive feedback of gain p. Such a system is graphically illustrated in Fig. 7(a), where the wavelength dependency is obviated to simplify the notation. In this diagram, the outer box represents the canopy scattering, the inner box represents the leaf scattering, and the feedback link represents the multiple scattering. If we further assume a negligible downward component of scattered photons and null leaf transmittance, then y corresponds to the canopy reflectance, i.e., the mixed spectrum, and x correspond to the leaf reflectance, i.e., the endmember spectrum.

The model was generalized here to consider multiple endmembers, e.g., when the homogeneous canopy has a non-dark background or when two or more canopies contribute to the mixed spectrum. The system diagram for the general case is shown in Fig. 7(b). In this model, the total incoming radiation is split into endmember interceptances (αs). Then, a single photon that has interacted with the ith endmember may interact with the jth endmember with probability p_{ij} or escape recollision with probability:

$$q_i = 1 - \sum_{j=1}^{m} p_{i,j} \tag{6}$$

Using the diagram of Fig. 7(b) and Eq. (6), the canopy reflectance yields Eq. (7), where $\alpha = [\alpha_1 \cdots \alpha_m]^T$ defines the proportion of light intercepted by each endmember, $\mathbf{X}(\lambda) = \mathbf{diag}[x_1(\lambda), \ldots, x_m(\lambda)]$ is a diagonal matrix of endmember spectra, $\mathbf{P} = [p_{ij}]_{i,j=1,\ldots,m}$ is termed the recollision probability matrix (RPM), and $\mathbf{I}$ is the identity matrix of order m:

$$y(\lambda) = (1 - \mathbf{P}1)^T \left[\mathbf{I} - \mathbf{X}(\lambda)\mathbf{P}^T\right]^{-1} \mathbf{X}(\lambda)\alpha \tag{7}$$

Eq. (7) is hereafter referred to as the multiple scattering approximation (MSA) model and, hence, Eq. (5) is the MSA model for one endmember (MSA-1). An explicit expression for the two-endmember model (MSA-2) is provided in Eq. (8):

$$y(\lambda) = \frac{\alpha_1 q_1 x_1(\lambda) + \alpha_2 q_2 x_2(\lambda) + K_1 x_1(\lambda) x_2(\lambda)}{1 - p_{1,1} x_1(\lambda) - p_{2,2} x_2(\lambda) + K_2 x_1(\lambda) x_2(\lambda)} \tag{8}$$

with constants $K_1 = \alpha_1(q_2 p_{1,2} - q_1 p_{2,2}) + \alpha_2(q_1 p_{2,1} - q_2 p_{1,1})$, $K_2 = p_{1,1}p_{2,2} - p_{2,1}p_{1,2}$, and q_1 and q_2 are defined by Eq. (6). Fig. 8 illustrates the mixing space using the MSA-2 model (Eq. (8)) on three wavebands. The surface is bounded by the linear mixing subspace at the top ($q_1 = q_2 = 1$) and by the shade point at the bottom ($q_1 = q_2 = 0$). As the escaping probabilities decrease, and for fixed interceptances, the mixed points describe nonlinear, yet smooth trajectories converging at the shade point.

It should be noted that if the RPM is zero, then the MSA model results in the linear model. If the RPM is diagonal, the MSA model results in a linear combination of multiple MSA-1 models. Furthermore, if the RPM is invariant across the landscape, the MSA model can be treated as a linear model with transformed endmembers. In practice, however, the recollision probabilities depend on the canopy structure, which may vary significantly even between vegetation canopies of the same species. For the case of a single homogenous canopy with a dark background, a theoretical expression for the dependence of recollision probability on leaf area index (LAI) had been derived from nesting recollision probabilities using Eq. (5) (Lewis & Disney, 2007). In this study, only the cases for one, two and three endmembers with varying recollision probabilities were considered.

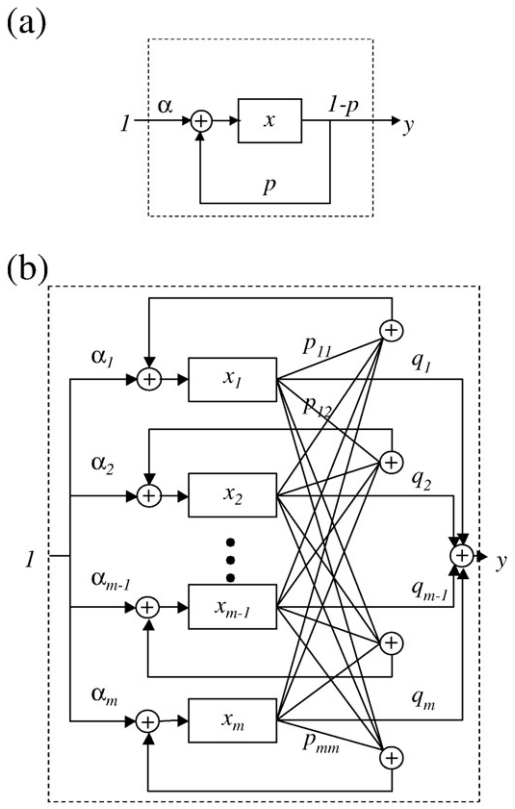

Fig. 7. These flow diagrams show the system-like representation of the multiple scattering approximation models for one endmember (a) and for m endmembers (b). The unit input indicates a normalized number of photons. Variables xs represent subcanopy endmember reflectance, whereas y represents the canopy reflectance. The canopy structural parameters are interceptances (αs), recollision probabilities (ps) and escaping probabilities (qs).

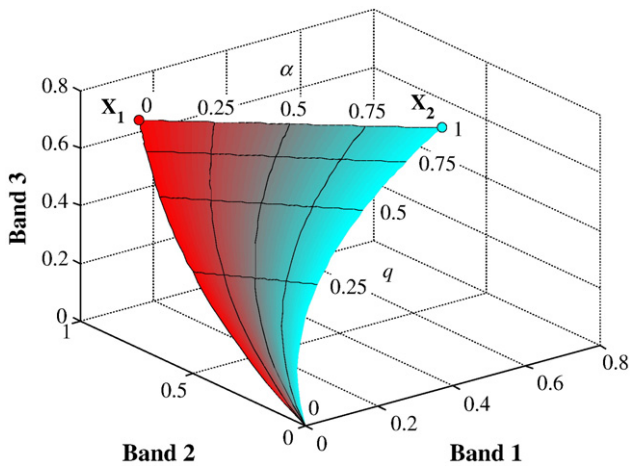

Fig. 8. Mixing space generated with a two-endmember multiple scattering approximation (MSA-2) model. Locations of endmembers are labeled as X_1 and X_2. Each point in the surface represents a mixed pixel and its color represents the relative contribution from each endmember (α for X_1 and $1-\alpha$ for X_2). The surface was generated from varying the endmember interceptance $\alpha = \alpha_1 = 1 - \alpha_2$ and the escaping probability $q = q_1 = q_2$, while fixing $p_{1,1} = p_{1,2} = p_{2,1} = p_{2,2} = 0.5(1-q)$. The surface is representative of the mixing space because the variation in the proportion of auto recollision ($p_{i,i}$) to inter recollision ($p_{i,j}$, $i \neq j$) did not produce significant deviations from the surface.

3.2.2. A fully constrained MSA spectral unmixing

The fully constrained MSA spectral unmixing method consisted of fitting directly the MSA model to Landsat reflectance measurements in order to estimate the wavelength independent parameters ($\mathbf{P}$ and α). In this case, the OLS approach was adopted so that the residual between the mixed spectra $\mathbf{y}$ and the model-synthesized spectra $\mathbf{y}_{\mathbf{P},\alpha}$ was minimized. The optimization problem is formally stated as follows:

$$\min_{\alpha,P} \|\mathbf{y}-\mathbf{y}_{\mathbf{P},\alpha}\|^2 \tag{9}$$

subject to:

$i)\ 1^T\alpha = 1$
$ii)\ \alpha \geq 0$
$iii)\ \mathbf{P}1 \leq 1$
$iv)\ \mathbf{P} \geq 0$

Since the MSA model is far more complex than the linear model, the optimization had to be solved numerically. A FMINCON function available in the optimization toolbox of MATLAB software was used with the medium-scale optimization option. FMINCON uses a sequential quadratic programming (SQP) method. At each iteration, the function solves a QP subproblem using an active set strategy (similar to that described by Gill et al., 1981). Initially, this method was meant to be tested using field measurements. Unfortunately, due to the spatial heterogeneity of subcanopy spectra, and to the computational burden of the optimization method, image spectra were considered instead. The optimization method was tested using the L1ETM library discussed in Section 3.1.2. The optimization algorithm required an initial solution, which was set to 1/3 for the three fractions and zero for the nine recollision probabilities. This method is hereafter simply referred to as MSA.

3.2.3. The tessellated MSA spectral unmixing method

A second method used MSA-1 and MSA-2 models to synthesize canopy spectra from subcanopy spectra. The synthesized spectra were used to create a new library referred to as the L2SYNTH spectral library (see Fig. 1 and Section 3.2.4). The L2SYNTH spectral library was then passed to the TLSU procedure (Section 3.1.3) with an aggregation matrix that weighted the contribution of each library spectrum according to the interceptances of subcanopy endmembers. For instance, if the linear spectral unmixing of a pixel yields a fraction of 0.70 for a simulated spectrum with 0.80 interceptance of saltcedar and 0.20 interceptance of grass, then the fractions of subcanopy endmembers assigned through the aggregation matrix are $0.7\times0.8=0.56$ for saltcedar and $0.7\times0.2=0.14$ for grass. The rationale of this method is that while the MSA model captures the nonlinearity between subcanopy and canopy reflectance, the linear unmixing accounts for the light integration at the scale of the sensor's field of view. This method is hereafter referred to as the tessellated MSA or TMSA.

3.2.4. The L2SYNTH spectral library

The L2SYNTH spectral library was formed using primarily synthesized canopy spectra from the MSA-1 and MSA-2 models. Fifteen subcanopy spectra were selected to serve as endmembers of the nonlinear models (Table 3). The selection process aimed to reduce the redundancy of measurements. Redundant spectra were identified in terms of the spectral angle among spectra of the same class, so that selected spectra differed from each other by no less than 3°. The values of auto recollision probabilities (p for MSA-1 or $p_{1,1}$ and $p_{2,2}$ for MSA-2) were selected within a range (p_{min}–$p_{\max}$) that was determined empirically from fitting the AISA spectra to field spectra. More specifically, scatter plots of subcanopy vs. canopy spectra of major woody riparian species were examined and fit to the MSA-1 and MSA-2 models. All possible one- and two-endmember combinations of subcanopy spectra were fit to each canopy spectra. Fitting results were inspected and models classified into plausible and non-plausible. A plausible model satisfied three criteria: 1) the spectral angle between model spectra and image spectra was under 3°, 2) at least one endmember, the dominant endmember, had interceptance of 0.7 or greater and 3) the class of the dominant endmember coincided with the class of the canopy spectra.

Table 3
Selected subcanopy spectra and quantization of recollision probabilities used for synthesizing canopy spectra with one- and two-endmembers multiple scattering approximation models (MSA-1 and MSA-2, respectively).

Target name (selected samples)	Recollision probabilities	
	$p_{\min}$–$p_{\max}$	Δ_p (MSA-1/MSA-2)
Green saltcedar (3)	0.6–0.9	0.15/0.3
Senescent saltcedar (2)	0.3–0.9	0.15/0.3
Dry saltcedar (2)	0.2–0.8	0.15/0.3
Leaf on mesquite (1)	0.1–0.5	0.1/0.2
Leaf-off mesquite (1)	0.1–0.3	0.1/0.2
Leaf on willow (1)	0.1–0.7	0.15/0.3
Leaf-off willow (1)	0.1–0.4	0.15/0.3
Poverty weed (2)	0.1–0.9	0.2/0.4
Creosote bush (1)	0.1–0.7	0.2/0.2
Grass (1)	0.0	0/0

Although the same range of values was used with MSA-1 and MSA-2, a coarser quantization (Δ_p) had to be used for MSA-2 due to the huge number of endmember–parameter combinations. Table 3 summarizes the range and quantization values for all field spectra. The values for inter recollision probabilities ($p_{1,2}$ and $p_{2,1}$) were selected in such a way that the escaping probabilities took the values of $1-p_{i,i}$, $(1-p_{i,i})/2$ and $(1-p_{i,i})/4$ for each value of $p_{i,i}$ considered. While the interceptance parameter of MSA-1 (α) was set to 1.0, interceptance parameters in MSA-2 (α_1 and α_2) were allowed to take values of 0.1, 0.3, 0.5, 0.7 and 0.9 (while fulfilling the sum-to-one constraint) for a strict two-endmember mixture.

Initially, all possible two-endmember mixtures were simulated with all parameter combinations. Upon subsequent crosschecking with field observations, some cases were excluded and additional combinations included. Combinations with creosote bush were excluded because that plant is unlikely to occur in mixed stands with the other species. In contrast, grass, water and soil are likely to occur in the under story of saltcedar, mesquite or willow species. Hence, AISA spectra for water and soil, with zero auto recollision probabilities, were also combined with the woody species using the MSA-2 model. Combinations of non-woody vegetation, such as grass–soil, water–grass, etc., were excluded as these are unlikely to undergo multiple scattering. Parameter combinations that yielded diagonal recollision probability matrices were also excluded because they can be represented as linear combinations of two MSA-1 models. The final number of two-endmember combinations yielded 28,530 spectra, plus 61 spectra from one-endmember combinations. In addition, 25 AISA spectra from non-vegetated land cover classes were included in the final library.

3.3. Methods of accuracy assessment

The performance of each unmixing method was assessed using the root mean square error (*RMSE*) criterion. Specifically, if $\tilde{\mathbf{y}}_k$ and $\mathbf{y}_k$ denote the estimated and actual reflectance spectra at pixel k, and $\tilde{\alpha}_k$ and α_k denote the estimated and actual subpixel fractions at pixel k, then the following error measures are defined on a per-pixel basis:

$$RMSE(\mathbf{y}_k,\tilde{\mathbf{y}}_k) = \sqrt{\frac{1}{n}\sum_{i=1}^{n}\left(y_{i,k}-\tilde{y}_{i,k}\right)^2} \tag{10}$$

and

$$RMSE(\alpha_k, \tilde{\alpha}_k) = \sqrt{\frac{1}{m}\sum_{j=1}^{m}\left(\alpha_{j,k} - \tilde{\alpha}_{j,k}\right)^2} \quad (11)$$

Average and standard deviation of *RMSE* measures were calculated from the test sample discussed in Section 2.4.

In addition, the subpixel confusion-uncertainty matrix (SCM) was calculated, and overall and per-class accuracy measures were derived (Silván-Cárdenas & Wang, 2008). The SCM provided detailed information on the source and type of errors, analogous to the traditional confusion matrix for crisp classifications. In general, the SCM consists of confusion intervals that quantify the uncertainty of subpixel confusions. However, since the classification system included only three classes, interclass confusions can be uniquely determined (Silván-Cárdenas & Wang, 2008). In this case, the confusion was quantified through the following composite operator:

$$C_{ij} = \begin{cases} \sum_k min\left(\tilde{\alpha}_{i,k}, \alpha_{j,k}\right) & \text{for } i = j \\ \sum_k \Delta\tilde{\alpha}_{i,k}\Delta\alpha_{j,k} \,/\, \sum_l \Delta\alpha_{l,k} & \text{for } i \neq j \end{cases} \quad (12)$$

where

$$\Delta\tilde{\alpha}_{i,k} = \tilde{\alpha}_{i,k} - min\left(\tilde{\alpha}_{i,k}, \alpha_{i,k}\right)$$

$$\Delta\alpha_{j,k} = \alpha_{j,k} - min\left(\tilde{\alpha}_{j,k}, \alpha_{j,k}\right)$$

denote the over- and underestimation errors of classes i and j at pixel k, respectively. For the calculation of the SCM, subpixel classification fractions were first trimmed to the unit interval and then normalized to sum to one on a per-pixel basis.

4. Results

4.1. Role of multiple scattering on canopy spectra

In order to search for evidence of the multiple scattering phenomena (objective 1) and its proper representation with the MSA model, canopy spectra were compared with subcanopy spectra. Average canopy and subcanopy spectra were projected onto the principal components plane PC1–PC2 that was generated from

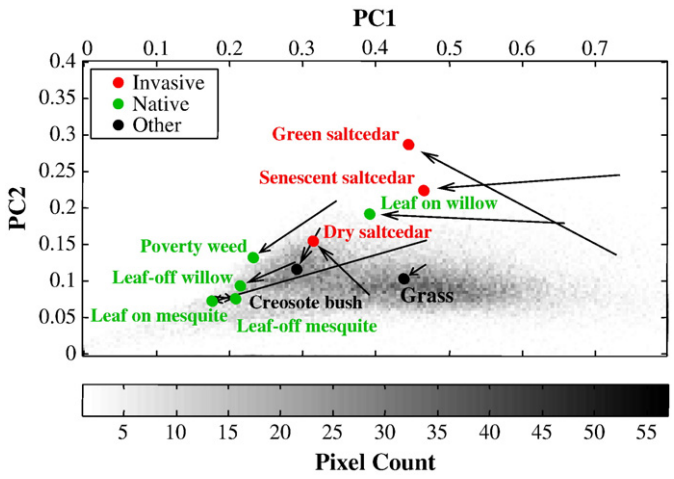

Fig. 9. Two dimensional scatterplot on the space spanned by two principal components (PC1 and PC2) of Landsat pixel cloud. The average locations of canopy reflectance are shown as filled circles. Arrows represent the displacement from average location of subcanopy spectra (branch/shoot level) to average location of canopy spectra. The background image represents pixel counts of Landsat pixels.

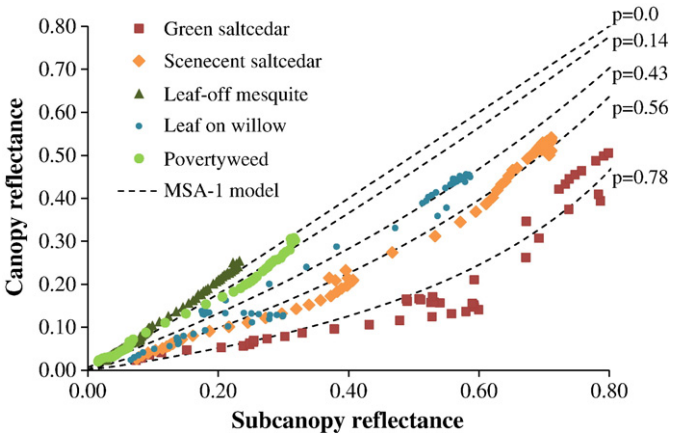

Fig. 10. Subcanopy vs. canopy reflectance scatterplot from spectral curves in Fig. 4. Discontinuous lines represent the least square fitting of the one-endmember multiple scattering approximation (MSA-1) model. Estimated recollision probabilities (p) are provided for each case.

Landsat mixed pixels (Fig. 9), and the displacement between the locations of subcanopy spectra to their corresponding locations of canopy spectra was inspected. If a canopy spectrum results from the mixture of subcanopy spectra as prescribed by the MSA model, then it is reasonable to expect a displacement vector pointing slightly towards the shadow point, but perhaps not straight to the shadow point (see Fig. 8). It was observed that all species, excluding leaf-off mesquite, had displacement vectors with a positive component pointing towards the origin (Fig. 9). Such a displacement should indicate an escaping probability under one (i.e., multiple scattering). Moreover, the greater the component of the displacement towards the origin, the smaller (larger) the escaping (recollision) probability should be. Consistently, leaf-off vegetation had small displacement vectors, whereas leaf-on vegetation showed the largest displacement indicating a higher effect from multiple scattering on canopy spectra.

In addition to the vector displacement analysis above, results from fitting the MSA-1 and MSA-2 models yielded least square estimates of recollision probabilities, which are summarized in Table 3. The estimated recollision probabilities were consistent with the vector displacement analysis above. The effect of multiple scattering was apparent in the attenuation of canopy reflectance with respect to subcanopy reflectance (see e.g., Fig. 10). Interestingly, canopies of green and senescent saltcedar tended to have a larger likelihood of photon recollision than all other species (Table 3). This was presumably due to its tiny, needle-like leaf (3 mm in length against 3 cm for mesquite), as well as its canopy structure.

4.2. Subpixel classification results

Maps of retrieved subpixel fractions from the top-five most accurate methods are provided in Fig. 11. The accuracy assessment results are discussed below in terms of the role of constraint level and endmember definition (objectives 2 and 3) as well as in terms of mixture model (objective 3).

4.2.1. Role of constraint level and endmember definition

In terms of the constraint levels considered for LSU, it was observed that the fitting error (*RMSE* of reflectance) increased for increasing levels of constraint. Nonetheless, the relatively low *RMSE* of reflectance spectra (less than 1% in most cases) indicated that all solutions fit the data fairly well (Table 4). In contrast, subpixel fraction estimation errors decreased with increasing levels of constraint. In this case, the nonnegativity constraint was found to be more important than the sum constraint, so FCLSU performed comparably with NCLSU. When fractions were renormalized to the unit interval,

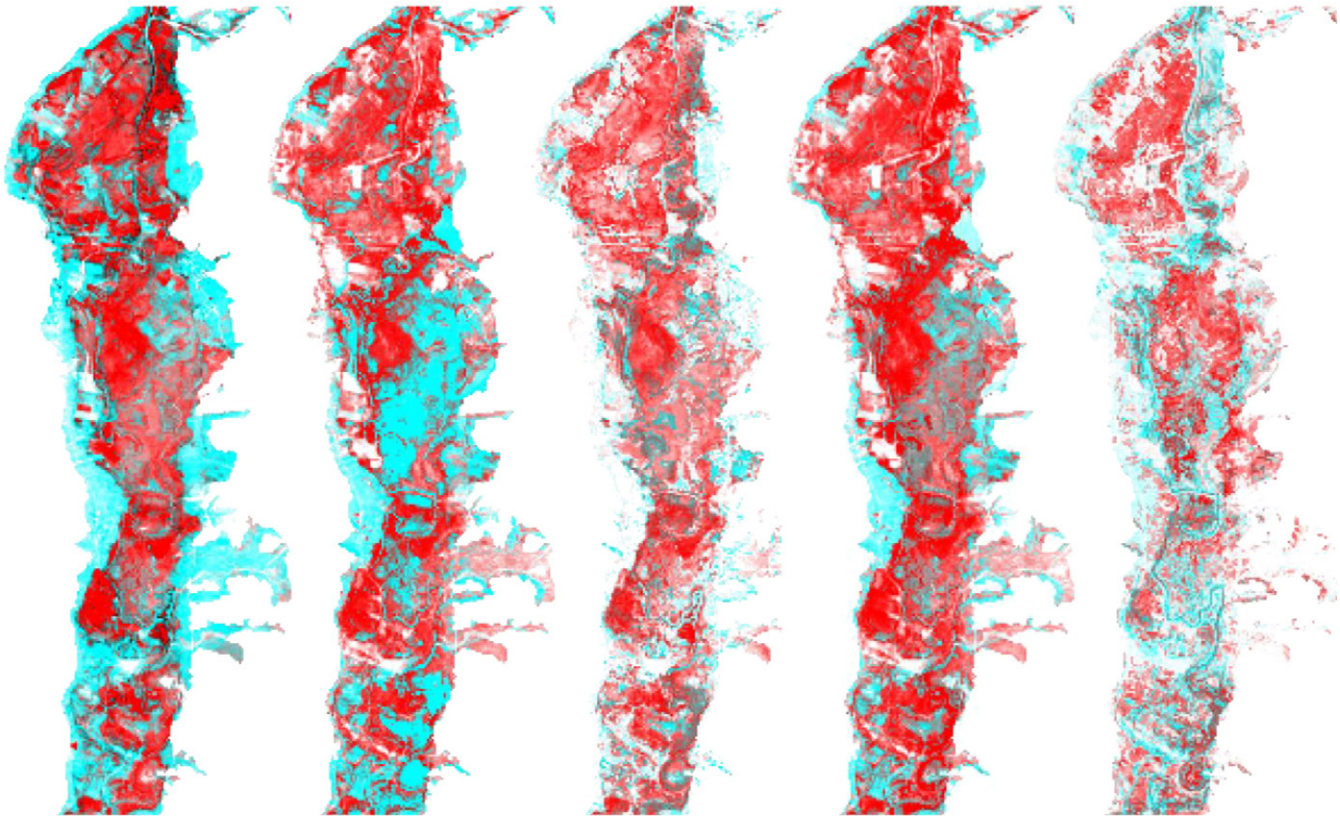

Fig. 11. Subpixel canopy cover retrieved from several methods. From left to right: NCLSU, FCLSU, TLSU, MSA and TMSA. Red tones correspond to invasive species, cyan tones correspond to native species. See Fig. 5 for reference fractions and color scale.

the subpixel classification accuracy improved for unconstrained and partially constrained methods (Table 5).

In addition to the constraint level, the thematic level of endmember definition seemed to have a significant effect on the final subpixel fractional estimation. The TLSU method (and also TMSA), which employed level 2 endmembers, showed superior performance over linear methods based on level 1 endmembers. This result is attributed to the fact that intra-class variability of spectral signatures was better represented by level 2 spectra.

4.2.2. Role of mixture model

Although linear mixing was expected to occur for image endmembers, MSA yielded the best result among methods that used endmember definition at thematic level 1. This result advocates for nonlinear mixing at a landscape level, which appears to be better represented by the MSA model than by the linear model. Nonetheless, the least square inversion of the MSA was sensitive to the initial solution. Some early tests using random initializations yielded poorer estimates of fractional cover (data not shown). The best result was found when the recollision probability matrix was initially set to zero, so the solution found through least square optimization resulted in a nearly linear mixture model. The proximity to linearity is indicated through the relatively low average recollision probabilities provided in Table 6.

For comparison of the linear and nonlinear spectral unmixing, Table 7 presents the confusion matrices and derived accuracy indices for FCLSU and MSA. One major difference between the two methods was the higher confusion of Native classified as Invasive by FCLSU (20.6%) with respect to MSA (1.5%). These confusion values led to higher producer accuracy of retrieved saltcedar from MSA (96.7%) than from FCLSU (78.8%). However, the user accuracy of saltcedar was the same for both methods (59.3%). The user accuracy indicated

Table 4
Root mean square error (*RMSE*) statistics of mixed reflectance and subpixel fractional land cover estimations by several spectral unmixing methods: unconstrained, sum-constrained, nonnegativity-constrained, fully constrained, and tesselated linear spectral unmixing (UCLSU, SCLSU, NCLSU, FCLSU and TLSU, respectively), and fully constrained and tesselated multiple scattering approximation spectral unmixing (MSA and TMSA, respectively).

Method	Average *RMSE* (standard dev.)	
	Reflectance [%]	Fractions [%]
UCLSU	0.2(0.2)	31.5(23)
SCLSU	0.7(0.7)	48.1(45)
NCLSU	0.4(0.6)	25.5(15)
FCLSU	1.3(1.8)	25.1(15)
TLSU	0.1(0.3)	16.9(11)
MSA	1.1(1.6)	20.8(13)
TMSA	0.0(0.3)	23.3(14)

Table 5
Overall accuracy, kappa statistics, and user and producer accuracies for class Invasive. Computations were based on renormalized fractional land cover estimations by several spectral unmixing methods: unconstrained, sum-constrained, nonnegativity-constrained, fully constrained, and tesselated linear spectral unmixing (UCLSU, SCLSU, NCLSU, FCLSU and TLSU, respectively), and fully constrained and tesselated multiple scattering approximation spectral unmixing (MSA and TMSA, respectively).

Method	Overall acc. (kappa)	User accuracy	Producer accuracy
UCLSU	72(0.57)	75	85
SCLSU	63(0.45)	54	84
NCLSU	72(0.58)	68	94
FCLSU	67(0.51)	59	79
TLSU	77(0.66)	78	90
MSA	73(0.59)	59	97
TMSA	69(0.53)	72	51

similar reliability of saltcedar canopy cover estimations from both methods.

Contrary to expectations, the TMSA method, which accounts for the nonlinear mixing of subcanopy spectra onto canopy spectra, performed under its linear counterpart (TLSU). Nonetheless, a close inspection of the errors yielded by TMSA revealed that the reference fractions could have favored methods based on image endmembers. The issue is the reference fractions were derived using image spectra selected from the AISA image. These image spectra should have been considered mixed spectra from subcanopy spectra.

Consistently, results from TMSA (Fig. 12) showed a trend from slight overestimation (under 20%) for low fractions to strong underestimation (around −60%) of higher fractions. Higher fractions imply a high canopy closure and, consequently, little or no direct light transmission to the ground. This is unlikely to happen in reality considering the small leaf sizes of both native and invasive species and the phenological stage at the time of image acquisition. If this were the case, then the actual subpixel class distribution would look more fragmented and mixed than that shown in Fig. 5. Fig. 11 (far right) shows the map derived from TMSA, which matches more closely the above description. Aside from errors in the reference data, other factors could have affected the performance of TMSA. These include, for instance, the use of a relatively coarse quantization of parameter values and the lack of a comprehensive spectral sample of the understory. Despite this, the subpixel classification accuracy through TMSA was among the top three considering the *RMSE* of fractions (Table 4). It was also among the top three methods in terms of reliability for saltcedar's subpixel canopy coverage estimation, as indicated through the user accuracy (Table 5).

5. Discussion

Results indicated that linear models can achieve higher accuracy when at least the nonnegativity constraint is imposed. Unfortunately, the consideration of such a constraint with the least square optimization may not be practical for a regional-scale mapping task due to the iterative nature of the algorithm (Heinz & Chang, 2001). The unconstrained solution with post-classification normalization can yield comparable accuracy to the nonnegative constrained method, with the advantage of being more efficient. The consideration of a nonlinear mixture model further increased the accuracy. However, the marginal improvement with respect to the best linear spectral unmixing method was not sufficient enough to justify the computational burden imposed by the nonlinear method. Although the use of aggregated endmembers can yield relatively high accuracy, its definition relied on knowledge of nearly pure pixels derived from the AISA image.

Per-species spectra collected through sampling the AISA image provided a better representation of the intrinsic variability of canopy spectra. The main problem faced in this case was the automatic selection of endmember spectra. An efficient solution based on

Table 6
Statistics of least square estimated recollision probabilities from the fully constrained multiple scattering approximation spectral unmixing method (MSA). $p_{i,j}$ represents the recollision probability from land cover class i to land cover class j, for the land cover classes 1 = Invasive, 2 = Native and 3 = Other.

Recollision probability	Min.	Max.	Avg.	Std. Dev.
$p_{1,1}$	0	0.54	0.06	0.11
$p_{2,1}$	0	0.45	0.04	0.08
$p_{3,1}$	0	0.43	0.06	0.08
$p_{2,1}$	0	0.49	0.03	0.08
$p_{2,2}$	0	1.00	0.05	0.12
$p_{2,3}$	0	0.30	0.06	0.08
$p_{3,1}$	0	0.29	0.02	0.04
$p_{3,2}$	0	0.31	0.02	0.05
$p_{3,3}$	0	0.42	0.07	0.10

Table 7
Subpixel confusion matrix for (a) fully constrained linear spectral unmixing (FCLSU) and (b) fully constrained multiple scattering approximation spectral unmixing (MSA), and (c) accuracy indices from each method.

Class	Reference (%)			Total
	1	2	3	
(a)				
1. Invasive	78.8	35.6	18.9	43.8
2. Native	20.6	62.9	21.7	34.0
3. Other	0.7	1.6	59.4	22.2
Total	100.0	100.0	100.0	100.0
(b)				
1. Invasive	96.7	45.6	21.7	53.8
2. Native	1.5	51.3	9.9	19.9
3. Other	1.8	3.1	68.4	26.3
Total	100.0	100.0	100.0	100.0

Class	FCLSU		MSA	
	Prod. acc.	User acc.	Prod. Acc.	User acc.
(c)				
Invasive	78.8	59.3	96.7	59.3
Native	62.9	57.0	51.3	79.5
Other	59.4	96.8	68.4	94.0
	$OA = 66.86\%$ ($\kappa = 0.5056$)		$OA = 72.46$ ($\kappa = 0.5865$)	

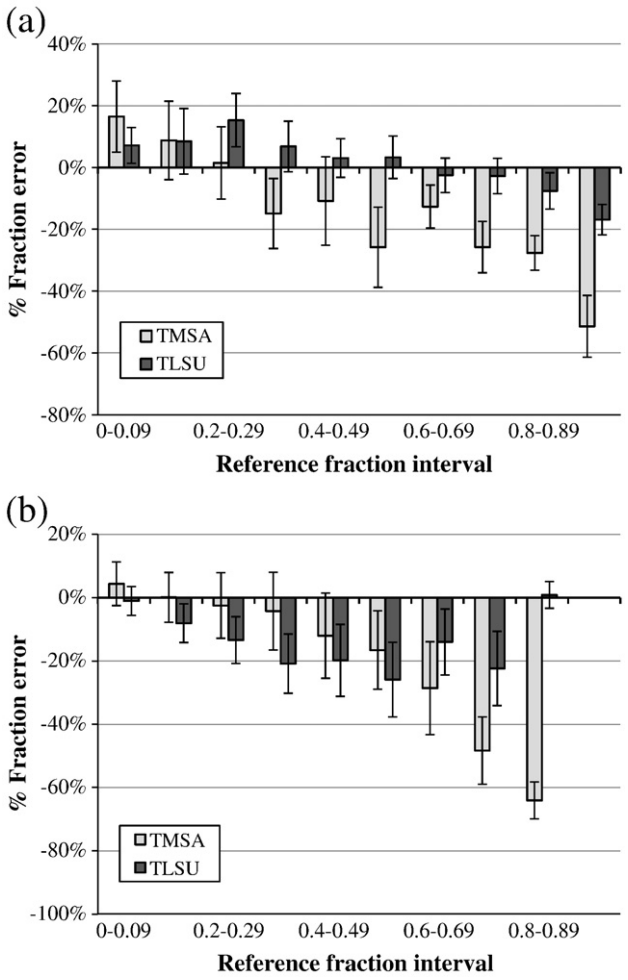

Fig. 12. Error bars from estimated fractions for Invasive (top) and Native (bottom) classes. Bars correspond to average errors within each reference fraction interval. The standard deviation for each interval is indicated with the length of the vertical line.

concepts of computational geometry was adopted. This method achieved the highest accuracy measures of all methods tested, presumably due to a better representation of intra-class spectral variability. The fact that the reference fractions and the endmember library had a common source, the hyperspectral imagery, may also have contributed to the superior performance of the TLSU method. One major limitation of this approach is the cost associated with acquisition of the hyperspectral image. Nevertheless, such costs are not significantly high considering that the spectral sampling and fraction derivation for accuracy assessment is only necessary for limited spatial extents, while the benefit of monitoring through Landsat imagery comes from considering wide spatial extents (e.g., a basin-wide area). A cheaper alternative would be using comprehensive top-of-canopy measurements from fieldwork in place of airborne measurements. Such datasets are, however, hard to collect and can lead to larger discrepancy with respect to image measurements due to differences in acquisition conditions (Plaza et al., 2004).

As an alternative to canopy endmembers, subcanopy reflectance measurements were considered. The linkage between subcanopy spectra and image spectra requires a nonlinear mixture model that accounts for the multiple scattering phenomena. A model rooted in spectral invariant theory (Huang et al., 2007; Lewis & Disney, 2007; Smolander & Stenberg, 2005; Stenberg, 2007) was proposed in this study. The matching of subcanopy reflectance spectra with canopy reflectance spectra provided evidence of a nonlinear relationship and allowed estimation of canopy recollision probabilities through least square model inversion. Results showed that leaf on trees had larger recollision probabilities than leaf-off trees. While variability of recollision probabilities was significant for most species, saltcedar trees generally yielded higher values (0.3–0.9), followed by willow (0.1–0.7) and mesquite (0.1–0.5). This result supported the hypothesis that effects from multiple scattering can be more significant for saltcedar canopies than for native species canopies.

The empirical recollision probability ranges were used to synthesize a large number of canopy spectra from one- and two-endmember combinations of subcanopy spectra. Since canopy spectra are more likely to undergo a linear mixing at the sensor's resolution (Roberts et al., 1993), it sufficed to apply the tessellated linear spectral unmixing of synthesized spectra to the Landsat image. The retrieved fractions of synthesized spectra were transformed back to fractions of subcanopy spectra. The accuracy of this method was moderate despite the large number of synthesized canopy spectra. Nonetheless, the accuracy measures may be more reliable provided that the reference fraction was derived from a totally independent source. This method may be cheaper to implement than the TLSU as it does not require the hyperspectral image for endmember definitions and measuring subcanopy reflectance is less tedious than measuring top-of-canopy spectra in the field. Furthermore, a method to measure the average value of the canopy recollision probability from canopy gap fraction data, which are provided for example by the LAI-2000 plant canopy analyzer (Stenberg, 2007), could be a reasonable alternative to the model fitting technique used here.

6. Conclusions

Moderate resolution remote sensing images, such as Landsat TM/ETM+, represent an attractive source of information for mapping the canopy cover of saltcedar and native species over wide extents at a low cost. In this study, seven spectral unmixing methods were tested on Landsat measurements for retrieving subpixel canopy cover of saltcedar and associated native species. A hyperspectral image was used derive reliable subpixel land cover fractions for accuracy assessment as well as for deriving canopy spectra to use as endmembers. Additionally, subcanopy reflectance measurements were acquired in the field. Based on these datasets, three endmember libraries were defined with varying level of detail.

Results indicated that: 1) When saltcedar was represented by one, single image spectrum (endmember), the unconstrained linear spectral unmixing with post-classification normalization produced comparable accuracy (OA = 72%) to those delivered by partially and fully constrained linear spectral unmixing (63–72%), and even by nonlinear spectral unmixing (73%). 2) The accuracy of the fully constrained linear spectral unmixing method increased (from 67% to 77%) when the classes were represented with several image spectra. 3) Saltcedar canopy reflectance showed the strongest nonlinear relationship with respect to subcanopy reflectance, as indicated through a range of estimated canopy recollision probabilities. 4) Despite the consideration of these effects on canopy reflectance, the inversion of the nonlinear spectral mixing model with subcanopy reflectance (field) measurements yielded slightly lower accuracy (73%) than the linear counterpart (77%).

The experiments presented in this study offer several avenues for further research. For instance, before any claim can be made about its explanatory power as model of canopy reflectance (or scattering), the MSA model should undergo more rigorous testing under controlled situations. One underlying assumption of the MSA model is that the reflectance spectra are continuous. This assumption is violated by the Landsat data used here. Hence, future work should also examine whether the consideration of a higher spectral resolution (i.e., hyperspectral data) coupled with the nonlinear mixture model could yield superior subpixel canopy cover retrieval than its linear counterpart.

Acknowledgments

The study was partly supported by grants to Le Wang from the National Science Foundation (DEB-0810933 and BCS-0822489), and from the US Department of Agriculture CSREES Award 2004-38899-02181). The final shape of the manuscript was achieved thanks to comments from five anonymous reviewers. The manuscript was proofread by Amy Frazier, a Ph.D. student at UB.

References

Adams, J. B., Smith, M. O., and Gillespie, A. R. (1993). Remote geochemical analysis: Elemental and mineralogical composition, chapter Imaging spectroscopy: Interpretation based on spectral mixture analysis, pages 145–166. Cambridge Univ. Press, MA.

Adams, J. B., Sabol, D. E., Kapos, V., Filho, R. A., Roberts, D. A., & Smith, M. O. (1995). Classification of multispectral images based on fractions of endmembers: Application to land-cover change in the Brazilian Amazon. *Remote Sensing of Environment*, *52*, 137−154.

Asner, G., & Heidebrecht, K. (2002). Spectral unmixing of vegetation, soil and dry carbon cover in arid regions: comparing multispectral and hyperspectral observations. *International Journal of Remote Sensing*, *23*(19), 3939−3958.

Barber, C., Dobkin, D., & Huhdanpaa, H. (1996). The quickhull algorithm for convex hulls. *ACM Transactions on Mathematical Software (TOMS)*, *22*(4), 469−483.

Bateson, C., Asner, G., & Wessman, C. (2000). Endmember bundles: A new approach to incorporating endmembervariability into spectral mixture analysis. *IEEE Transactions on Geoscience and Remote Sensing*, *38*(2 Part 2), 1083−1094.

Boardman, J., et al. (1993). Automating spectral unmixing of AVIRIS data using convex geometry concepts. *Summaries of the fourth annual JPL Airborne Geoscience workshop* (pp. 11−14).

Borel, C., & Gerstl, S. (1994). Nonlinear spectral mixing models for vegetative and soil surfaces. *Remote Sensing of Environment*, *47*, 403−416.

Carpenter, G. A., Gopal, S., Martens, S., & Woodcock, C. E. (1999). A neural network method for mixture estimation for vegetation mapping. *Remote Sensing of Environment*, *70*, 138−152.

Carruthers, R., Anderson, G., DeLoach, J., Knight, J., Ge, S., & Gong, P. (2006). Remote sensing of saltcedar biological control effectiveness. *USDA Forest Service* (pp. 50−56).

Chang, C. -I., & Heinz, D. C. (2000). Constrained sub-pixel target detection of remotely sensed imagery. *IEEE Transaction on Geoscience and Remote Sensing*, *38*(3), 1114−1159.

Dennison, P., & Roberts, D. (2003). Endmember selection for multiple endmember spectral mixture analysis using endmember average RMSE. *Remote Sensing of Environment*, *87*(2), 123−135.

Drake, J. A., Mooney, H. A., Castri, F. D., Groves, R. H., Kruger, F. J., Aejmamek, M., & Williamson, M. (1989). *Biological invasions: A global perspective.* Chichester: John Wiley & Sons.

Eastman, J., & Laney, R. (2002). Bayesian soft classification for sub-pixel analysis: A critical evaluation. *Photogrammetric Engineering and Remote Sensing*, *68*(11), 1149−1154.

Everitt, B. L. (1998). Chronology of the spread of tamarisk in the central Rio Grande. *Wetlands*, *18*(4), 658−668.

Everitt, J. H., & DeLoach, C. J. (1990). Remote sensing of Chinese tamarisk (*Tamarix chinensis*) and associated vegetation. *Weed Science*, *38*, 273−278.

Everitt, J. H., Escobar, D. E., Alaniz, M. A., Villareal, R., & Davis, M. R. (1992). Distinguishing brush and weeds on rangelands using video remote sensing. *Weed Technology*, *6*, 913−921.

Everitt, J. H., Escobar, D. E., Alaniz, M. A., Davis, M. R., & Richerson, J. V. (1996). Using spatial information technologies to map Chinese tamarisk (*Tamarix chinensis*) infestations. *Weed Science*, *44*, 194−201.

Gill, P., Murray, W., & Wright, M. (1981). *Practical optimization.* London: Academic Press.

Gill, P., Murray, W., & Wright, M. (1991). *Numerical linear algebra and optimization, volume 1.* Redwood City, CA: Addison-Wesley.

Gillespie, A. R. (1992). Spectral mixture analysis of multi-spectral thermal infrared images. *Remote Sensing of Evironment*, *42*, 137−145.

Groeneveld, D., & Watson, R. (2008). Near-infrared discrimination of leafless saltcedar in wintertime Landsat TM. *International Journal of Remote Sensing*, *29*(12), 3577−3588.

Hamada, Y., Stow, D. A., Coulter, L. L., Jafolla, J. C., & Hendricks, L. W. (2007). Detecting tamarisk species (*Tamarix* spp.) in riparian habitats of Southern California using high spatial resolution hyperspectral imagery. *Remote Sensing of Environment*, *109*, 237−248.

Heinz, D. C., & Chang, C. -I. (2001). Fully constrained least square linear spectral unmixing analysis method for matherial quantification in hyperspectral imagery. *IEEE Transactions on Geoscience and Remote Sensing*, *39*(3), 529−545.

Hu, Y. H., Lee, H. B., & Scarpace, F. L. (1999). Optimal linear spectral unmixing. *IEEE Transactions on Geoscience and Remote Sensing*, *37*(1), 639−644.

Huang, D., Knyazikhin, Y., Dickinson, R. E., Rautianen, M., Stenberg, P., Disney, M., Lewis, P., Cescatti, A., Tian, Y., Verhoef, W., Martonchik, J. V., & Myneni, R. B. (2007). Canopy spectral invariants for remote sensing and model applications. *Remote Sensing of Environment*, *106*, 106−122.

Hunt, E. R., Everitt, J. H., Ritchie, J. C., Moran, M. S., Booth, D. T., Anderson, G. L., Clark, P. E., & Seyfried, M. S. (2003). Application and research using remote sensing for range management. *Photogrammetric Engineering & Remote Sensing*, *69*(6), 675−693.

JJ, S., & Drake, N. (1993). Linear mixing and the estimation of ground cover proportions. *International Journal of Remote Sensing*, *14*(6), 1159−1177.

Keshava, N., & Mustard, J. F. (2002). Spectral unmixing. *IEEE Signal Processing Magazine*, *19*(1), 44−57.

Knyazikhin, Y., Martonchik, J., Myneni, R., Diner, D., & Running, S. (1998). Synergistic algorithm for estimating vegetation canopy leaf area index and fraction of absorbed photosynthetically active radiation from MODIS and MISR data. *Journal of Geophysical Research*, *103*(D24), 32257−32276.

Kruse, F. A., Lefkoff, A. B., Boardman, J. B., Heidebrecht, K. B., Shapiro, A. T., Barloon, P. J., & Goetz, A. F. H. (1993). The spectral image processing system (SIPS) — interactive visualization and analysis of imaging spectrometer data. *Remote Sensing of Environment*, *44*, 145−163.

Lass, L. W., Prather, T. S., Glenn, N. F., Weber, K. T., Mundt, J. T., & Pettingill, J. (2005). A review of remote sensing of invasive weeds and example of the early detection of spotted knapweed (*Centaurea maculosa* and babysbreath (*Gypsophila paniculata*) with a hyperspectral sensor. *Weed Science*, *53*, 242−251.

Lawson, C., & Hanson, R. (1974). Solving least squares problems.

Lewis, P., & Disney, M. (2007). Spectral invariants and scattering across multiple scales from within-leaf to canopy. *Remote Sensing of Environment*, *109*, 196−206.

Miao, X., Gong, P., Swope, S., Ruiliang, P., Carruthers, R., Anderson, A., Heaton, J. S., & Tracy, C. R. (2006). Estimation of yellow starthisle abundance through CASI-2 hyperspectral imagery using linear spectral mixture models. *Remote Sensing of Environment*, *101*, 329−341.

Milton, E. J. (1999). Image endmembers and the scene model. *Canadian Journal of Remote Sensing*, *25*(2), 112−120.

Morisette, J. T., Jarnevich, C. S., Ullah, A., Cai, W., Pedelty, J. A., Gentle, J. E., Stohlgren, T. J., & Schnase, J. L. (2006). A tamarisk habitat suitability map for the continental United States. *Front Ecol Environ*, *4*(1), 11−17.

Okin, G., Murray, B., Roberts, D., & Okin, W. (2001). Practical limits on hyperspectral vegetation discrimination in arid and semiarid environments. *Remote Sensing of Environment*, *77*(2), 212−225.

Plaza, A., Perez, P., & Plaza, J. (2004). A quantitative and comparative analysis of endmember extraction algorithms from hyperspectral data. *IEEE transactions on Geoscience and Remote Sensing*, *42*(3), 650−663.

Ravishanker, N., & Dey, D. (2002). *A first course in linear model theory, volume xvi.* Boca Raton: Chapman and Hall/CRC.

Ray, T., & Murray, B. (1996). Nonlinear spectral mixing in desert vegetation. *Remote sensing of environment*, *55*, 59−64.

Roberts, D., Smith, M., Sabol, D., Adams, J., & Ustin, S. (1992). Mapping the spectral variability in photosynthetic and non-photosynthetic vegetation, soils, and shade using AVIRIS. *Annual JPL Airborne Geoscience Workshop*, *Vol. 1.* (pp. 38−40).

Roberts, D. A., Smith, M. O., & Adams, J. B. (1993). Green vegetation, non-photosynthetic vegetation and soils in AVIRIS data. *Remote Sensing of Environment*, *44*, 255−269.

Roberts, D., Gardner, M., Church, R., Ustin, S., Scheer, G., & Green, R. (1998). Mapping chaparral in the Santa Monica Mountains using multiple endmember spectral mixture models. *Remote Sensing of Environment*, *65*(3), 267−279.

Shafroth, P. B., Cleverly, J. R., Dudley, T. L., Taylor, J. P., Van Riper, C., III, Weeks, E. P., & Stuart, J. N. (2005). Control of tamarix in the Western United States: Implications for water salvage, wildlife use, and riparian restoration. *Environmental Management*, *35*(3), 231−246.

Sher, A. A., Marshall, D. L., & Taylor, J. P. (2002). Establishmet pattern of native *Populus* and *Salix* in the presence of invasive nonnative *Tamarix*. *Ecological Applications*, *12*(3), 760−772.

Silván-Cárdenas, J. L., & Wang, L. (2008). Sub-pixel confusion-uncertainty matrix for the assessment of soft classifications. *Remote Sensing of Environment*, *112*, 1081−1095.

Small, C. (2004). The landsat ETM+ spectral mixing space. *Remote Sensing of Environment*, *93*, 1−17.

Smith, M., Adams, J., and Sabol, D. (1994). Imaging spectrometry — A tool for environmental observations, chapter Spectral mixture analysis — New strategies for the analysis of multispectral data, pages 125–143. Springer, Belgium: Brussels.

Smolander, S., & Stenberg, P. (2003). A method to account for shoot scale clumping in coniferous canopy reflectance models. *Remote Sensing of Environment*, *88*(4), 363−373.

Smolander, S., & Stenberg, P. (2005). Simple parameterizations of the radiation budget of uniform broadleaved and coniferous canopies. *Remote Sensing of Environment*, *94*, 355−363.

Stenberg, P. (2007). Simple analytical formula for calculating average photon recollision probability in vegetation canopies. *Remote Sensing of Environment*, *109*(2), 221−224.

Vitousek, P. M., D'Antonio, C. M., Loope, L. L., & Westbrooks, R. (1996). Biological invasions as global environmental change. *American Scientist*, *84*(5), 468−478.